ELSEVIER

Journal of Atmospheric and Solar-Terrestrial Physics 66 (2004) 807–824

Journal of ATMOSPHERIC AND SOLAR-TERRESTRIAL PHYSICS

www.elsevier.com/locate/jastp

The convergence of magnetospheric energy flux in the polar atmosphere

Jeffrey P. Thayer*, Joshua Semeter

SRI International, Menlo Park, CA, USA

Accepted 13 January 2004

Abstract

The upper atmosphere is strongly influenced by the convergence of energy, mass, and momentum flux from coupled but distant regions. In the polar regions, these sources include not only wave fluxes from the lower atmosphere and vacuum ultraviolet fluxes from the sun, but also fluxes of electromagnetic and kinetic energy of magnetospheric origin. Magnetospheric fluxes can constitute the dominant energy fluxes received by the polar atmosphere above 80 km. The way that the upper atmosphere responds to these sources depends on the upper atmospheric state, the type of energy source impacting the upper atmosphere, and the source's spatial and temporal scale. Furthermore, the upper atmosphere and ionosphere are electrodynamically and intertially coupled to the magnetospheric energy sources, such that the source type, its magnitude, and its structure can be altered by the condition and response of the polar upper atmosphere. It is the intention of this paper to elaborate on this complex interplay between the magnetosphere and the polar regions, with an emphasis on the polar aeronomic behavior and its influence on the magnetospheric sources.

Keywords: Polar; Upper atmosphere; Aurora; Poynting flux

1. Introduction

The transition from a collisionless plasma to a collision-dominated gas in the Earth's upper atmosphere occurs over a relatively short altitude range, largely between 80 and 200 km. At altitudes above 200 km, where $\nu_{in} \ll \Omega_i$ and $\nu_{en} \ll \Omega_e$, the ion and electron equations of motion perpendicular to the magnetic field reduce to the 'frozen-in-magnetic-flux" condition of plasma drifting together in the $E \times B$ direction on a common flux tube. Descending in altitude, the number of ion and electron collisions with the neutral gas increases. Even though the electron–neutral collision frequency is at least an order of magnitude greater than ion–neutral collision frequency, it is the ions that feel the initial effects of the neutrals and break their ties with the magnetic field. This is the case because the ion gyrofrequency is only slightly above 100 rad/s, while the electron gyrofrequency is 10^7 rad/s. It is when the ratio of the collision frequency to the gyrofrequency approaches or exceeds the value of one that the frozen-in condition is strongly violated. For ions, this occurs below about 200 km, while the electrons do not experience a significant departure from the $E \times B$ direction until about 80 km. Thus, this region represents a transition for the plasma where the influence of the magnetic field lines ends and the influence of the neutral gas begins.

This transition region is also host to the convergence of electromagnetic and kinetic energy (KE) provided by the magnetosphere. The convergence signifies a change in magnetospheric energy to other forms, such as photons, heat, and momentum. This conversion process is clearly illuminated by the aurora. Fig. 1a shows an auroral display over Sondrestrom, Greenland. The processed image in Fig. 1b shows the orientation of the magnetic field lines and the abrupt cessation of auroral photons, due to the exponentially increasing number of collisions with the neutral gas.

* Corresponding author. Tel.: +1-650-859-3557; fax: +1-650-859-3557/322-2318.

E-mail address: thayer@srl.com (J.P. Thayer).

1364-6826/$ - see front matter © 2004 Elsevier Ltd. All rights reserved.
doi:10.1016/j.jastp.2004.01.035

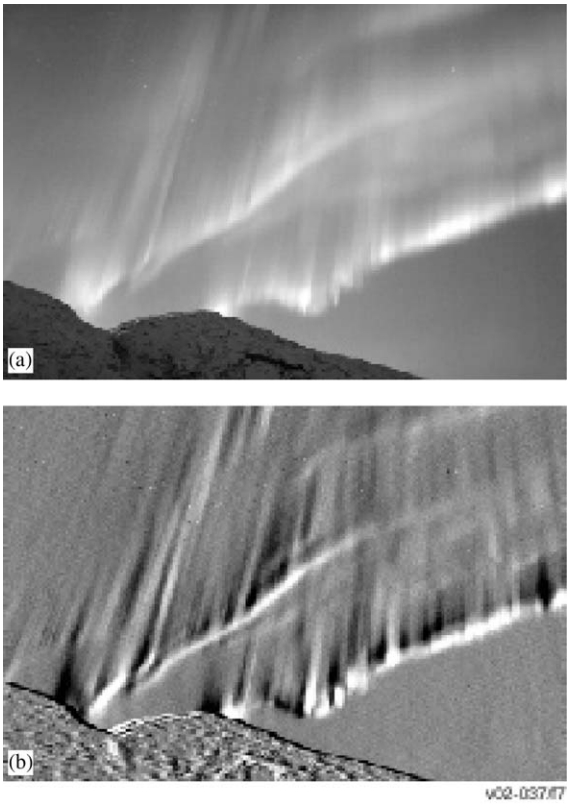

Fig. 1. An auroral display (a) a photograph and (b) a processed image that illustrates the field-aligned structure in the aurora.

The basic physics pertaining to plasma–neutral interactions in the Earth's ionosphere and thermosphere has been discussed in many books and journal articles (see Rishbeth and Garriott, 1969; Kelley, 1989; Brekke, 1997). The fundamental transport equations of energy, mass, and momentum for the ionosphere and thermosphere have also been well described by Banks and Kockarts (1973) and Schunk and Nagy (2000), for example. However, an adequate description of the mass, momentum, and energy coupling between the ionosphere–thermosphere (IT) and the magnetosphere, particularly at high latitudes, is still lacking. For many years the polar ionosphere was considered to be a passive recipient of magnetospheric energy, with the magnetosphere alone determining how much energy to transfer to the ionosphere. However, new observational evidence is bringing to light the fact that the polar IT system is an active participant in determining how much magnetospheric energy is transferred to the IT system. This raises the issue that is the central theme of this paper: How does the state of the polar IT system influence magnetospheric energy flux?

The paper is organized as follows. In Section 2 we review the concepts of flux and flux convergence as they pertain to the IT system. In Section 3 we describe the electromagnetic (EM) energy flux in terms of Poynting's theorem and show how it relates to the aeronomic properties of the ionosphere and thermosphere. In Section 4 we discuss the convergence of Poynting's flux, its altitude distribution through the ionosphere, and the importance of the aeronomic response to the partitioning of energy into heat and momentum. In Section 5 we present a description of the KE flux associated with accelerated electrons and their aeronomic impact through its convergence of flux in the thermosphere. In Section 6 we discuss the interplay between the magnetospheric Poynting flux and KE flux through mathematical relationships and observations. In the final section we summarize the paper, highlighting the salient points raised in each section.

2. The polar upper atmosphere: a system in flux

The polar atmosphere in the 80–200 km altitude range is subject to fluxes of energy from a variety of distant sources. This energy may be transported by gravity waves from the lower atmosphere, by solar radiation, by accelerated electrons and protons from the magnetosphere, or by the EM energy flux produced from magnetosphere–solar wind interactions. Regardless of their magnitude, these fluxes do not alter the atmospheric state unless they converge. Recall that a flux is a vector quantity whose convergence within a specified volume represents an interaction with the medium, resulting in a reduction in flux upon its exit. This basic concept has important consequences in recognizing what sources, or more importantly what portion of the source spectrum, influences the upper atmosphere.

A simple example is solar radiation. The irradiance, or energy flux, from the sun is greatest at visible wavelengths near 500 nm. But these visible wavelengths pass through the upper atmosphere with little convergence and little impact on the region. It is only at wavelengths shortward of about 200 nm—called the solar vacuum ultraviolet (VUV) that includes the Schumann–Runge continuum (from 175 to 105 nm), the lyman alpha band near 121 nm, the extreme ultraviolet (EUV, from 30 to 105 nm), and the soft X-ray (XUV, from 0 to 30 nm) portions of the spectrum—that the upper atmosphere responds. The net energy flux shortward of 200 nm is ~ 4 orders of magnitude less than at visible wavelengths (e.g., Tobiska et al., 2000), but the flux convergence at these wavelengths maximizes between 80 and 200 km altitude.

The VUV flux is also highly variable in time, and thus has a variable impact on the thermosphere and ionosphere, affecting such processes as photoionization and thermal dissipation. The significance of this variability in this portion of the source spectrum cannot be understated, as recently exemplified by Solomon et al. (2001) and references therein. Through recent measurements of soft X-ray irradiances, Solomon et al. have proposed a factor of four increase in the widely used solar XUV flux of Hinteregger et al. (1981), shortward of 25 nm. Using this increase in flux, Solomon et al. brought into agreement a long-standing discrepancy between middle-latitude incoherent scatter

radar measurements of electron density and photoionization models of the ionosphere.

While solar irradiance is often assumed to be the dominant source of energy in the sunlit thermosphere, auroral KE flux and EM energy flux can be of comparable magnitude at polar latitudes, adding an interesting degree of complexity to the system.

Fig. 2 shows curves of energy deposition rate (equivalent to negative energy flux divergence) in $\mu W/m^3$ for VUV, KE, and EM flux over a typical range of known variability. The solar VUV flux used in the calculations are from data taken by the SEE instrument on the TIMED spacecraft for July 4, 2002. The solar VUV deposition curve has been computed using the glow model (Solomon et al., 1988, 2001) for the Sondrestrom, Greenland location (67°N latitude) at local noon during summer solstice (solar zenith angle of 44°). These conditions correspond to the maximum expected deposition of solar flux at this location. The total vertical attenuated flux was about 8.3 mW/m^2, with 88% of the total attenuation (7.3 mW/m^2) occurring below 200 km. (By comparison, a calculation by Torr et al. (1980) for solar minimum and 60° solar zenith angle produced an energy flux estimate of 1.5 mW/m^2.) The energy is distributed broadly with a peak attenuation occurring below 120 km, primarily due to photodissociation of O_2 by the Schumann–Runge continuum.

Also shown in Fig. 2 is the deposition rate of EM energy flux, computed for three different values of electric field and a typical electron density profile measured by the Sondrestrom incoherent scatter radar for noontime, summer solstice, solar maximum conditions (taken July 13, 2001). The plotted quantity is $\sigma_p E^2$, where σ_p is the Pedersen conductivity and E is electric field magnitude. This quantity gives the EM deposition rate in the absence of neutral wind effects (discussed further in Section 4). The curves peak at about 120 km and have a slope similar to the VUV deposition curve above the peak. The shape of the curves is dictated by the Pedersen conductivity. The peak at about 120 km corresponds to the altitude where the ion–neutral collision frequency and the ion gyrofrequency are equal.

At 20 mV/m the total EM flux and the total solar VUV flux deposited below 200 km are comparable (EM flux ~ 5 mW/m^2), and have similar altitude distributions above 120 km. Electric fields of 20 mV/m are quite common and can extend throughout the entire sunlit high-latitude ionosphere. Thus, the net energy deposited by EM flux can be comparable to the net energy deposited by solar VUV flux in the polar ionosphere, with the majority of this energy being deposited at E-region altitudes. During active times, the electric field at high latitudes can easily reach values exceeding 60 mV/m, in which case the EM deposition rate can exceed the solar energy deposition rate at nearly all altitudes below 200 km.

Although the shape of the EM deposition curve is relatively invariant, the shape of the KE deposition curve depends strongly on the spectrum of energies in the incident particle beam (discussed further in Section 5). Fig. 2 includes two representative curves of auroral KE deposition. These correspond to the two higher-energy distributions in Fig. 5a of this paper (the lowest energy curve in Fig. 5a deposits less than 1% of its energy in this altitude range).

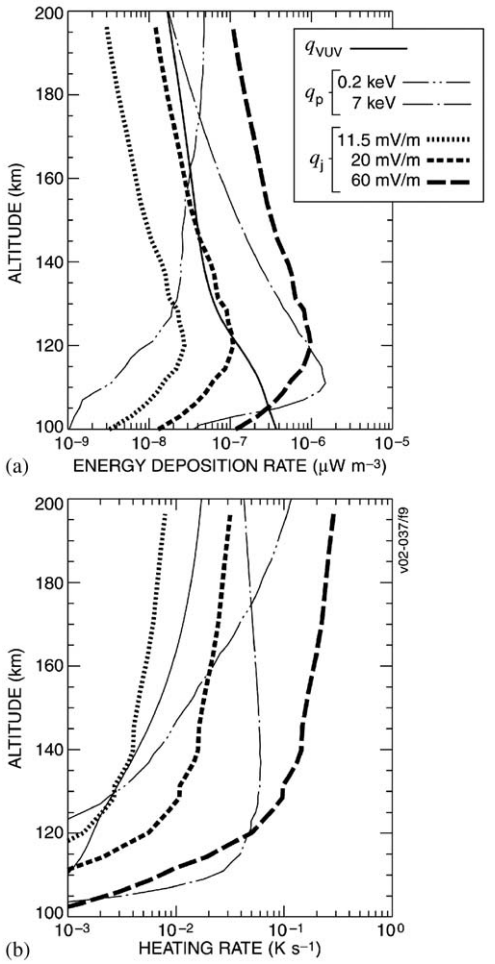

Fig. 2. (a) Height profiles of energy deposition rates for solar VUV flux, EM energy flux, and KE flux. The solar VUV energy deposition rate (q_{VUV}) is for summer solstice, solar maximum conditions with a solar zenith angle of 44°. The height-integrated VUV energy deposition rate from 80 to 200 km is 8.3 mW/m^2. The EM energy deposition rate (q_j) is for solar maximum, summer solstice conditions with electric fields of 11.5, 20, and 60 mV/m. Height-integrating q_j from 80 to 200 km results in energy fluxes of 1.7, 5.1, and 46.3 mW/m^2 for their respective electric fields. The deposition rate of KE flux (q_p) is for characteristic energies of 200 eV and 7 keV. The height-integrated q_p from 80 to 200 km is 2.5 mW/m^2 and 35.3 mW/m^2 for their respective characteristic energies. (b) Height profiles of neutral gas heating rates derived from the energy deposition rates given in graph a. The heating efficiency factors of 1.0 and 0.5 were used for the EM and KE fluxes. A factor of 0.45 was used for solar flux shortward of 105 nm and 0.3 for solar flux between 105 and 175 nm.

The curve peaking at 110 km corresponds to an accelerated electron distribution with a characteristic energy of ~7 keV and a total KE flux of 36 mW/m^2, typical of moderately bright, visible aurora. For this relatively hard spectrum, 98% (35.3 mW/m^2) of the net energy is deposited below 200 km. In comparison with the EM curves, this curve has a steeper bottomside scale height and peaks at a lower altitude.

The other KE deposition curve corresponds to a distribution with characteristic energy of ~200 eV and a total energy flux of 7 mW/m^2. For this softer distribution only 36% (2.5 mW/m^2) of the net energy flux is deposited below 200 km. An interesting point is that the difference between the two auroral deposition curves decreases with altitude, crossing over ~170 km. Soft electron precipitation preferentially enhances Pedersen conductance over the Hall conductance and can, thus, affect the dissipation of EM energy flux significantly despite carrying little KE flux.

Each of the sources plotted in Fig. 2 contributes to heating the neutral gas. In the case of auroral precipitation, the heating efficiency is a constant value of ~ 50% for altitudes below about 200 km (independent of the energy flux or characteristic energy) (Rees et al., 1983). Thus, the auroral energy lost to heat at a given altitude is obtained by simply multiplying the auroral curves in Fig. 2 by the factor 0.5. The heating efficiency for solar VUV flux monotonically increases from 30% in the lower E region to 50–60% in the upper E region, as shown by Torr et al. (1980), but the actual altitude profile depends on the solar cycle through its influence on thermospheric density and composition. A neutral gas heating efficiency is generally not applied to EM energy flux. It is typically assumed that all the flux is dissipated as the Joule heating to the neutral gas. However, it is clear that some energy is transferred to the momentum of the neutral gas to produce the observed wind behavior at high latitudes. This will be discussed in greater detail in Section 3.

Throughout this discussion we have described the energy deposition rates in units of energy per time per volume. However, atmospheric mass density decreases exponentially with height, and consequently, less energy per unit volume per unit time deposited at higher altitudes can have a significant impact on those fewer gas molecules and atoms. Thus, it is possibly more intuitive to convert these energy deposition rates to heating rates in Kelvins per second. To do so, we invoke the first law of thermodynamics such that the neutral gas heating rate is written as $\varepsilon q/\rho c_p$, where c_p is the specific heat of the gas at constant pressure ($m^2/s^2/K$), ρ is the mass density (kg/m^3), q is the energy deposition rate (W/m^3), and ε is the heating efficiency factor. Fig. 2b displays the heating rates for the energy deposition rates shown in Fig. 2a. It is clear that weak EM and KE fluxes produce comparable heating rates to the solar VUV flux. As the EM and KE fluxes increase, their heating contribution becomes significant, particularly below 140 km. The magnitude of the temperature perturbation rests on the persistence and activity level of the EM and KE fluxes.

An important point is that in the above discussion, we have only considered heat production, not heat loss. To derive the actual thermospheric temperature requires solving an appropriate equation of energy balance (e.g., Schunk, 1975) which, for the thermosphere, would include radiative cooling, adiabatic cooling by vertical winds induced by local heating, and heat conduction.

Although the deposition rates of VUV, KE, and EM energy can have comparable magnitudes in the 100–200 km altitude range, there are critical differences in how these fluxes transfer their energy to the medium. EM flux, for instance, is deposited largely as heat in the neutral gas, while for solar VUV and KE fluxes nearly half of the energy is lost to ionizing reactions, molecular dissociation and airglow. Interestingly, the ionization caused by precipitating particles leads to cooling by producing significantly more nitric oxide (NO), which can efficiently radiate infrared energy to space (Kockarts, 1980). Indirectly, the EM flux also contributes to the production of NO through the nonlinear temperature-dependent reaction of N(^{4}S) with molecular oxygen, but in much less proportion than through particle precipitation (see Roble et al., 1987; Siskind et al., 1989a, b).

The different ways of processing these energy sources can also lead to important mutual interactions among the fluxes, altering not only how and where the energy is deposited, but possibly the source itself. For instance, in their study of 9 years of DMSP satellite measurements, Newell et al. (1996) found that intense aurora is more likely to occur in darkness than in sunlight. This result demonstrates that the sunlit ionosphere influences the efficacy with which the aurora forms (i.e., the partitioning of EM flux and KE flux delivered by the magnetosphere). The precise mechanism by which this occurs has not yet been established. Such mutual interactions among VUV, EM, and KE flux continues to be an active topic within the community concerned with magnetosphere–ionosphere (MI) coupling. The topic will be discussed further in Section 6.

The long polar winters void of sunlight leave the EM and KE fluxes as the primary sources of energy flux at high latitudes. The magnitude of these continuous fluxes can vary on time scales from hours to seconds and over spatial scales from thousands of kilometers to tens of meters. In the following sections, we will focus on the magnetospheric energy fluxes prevalent in the polar regions and address the M–I coupling issues related to EM energy and KE flux and the IT aeronomic issues related to their convergence.

3. EM energy flux into the polar IT system

EM energy flux represents the flow of EM energy per unit time across a unit area perpendicular to the flow, and is often termed the Poynting flux. These synonymous terms originate from the conservation equation of EM energy derived directly from Maxwell's equations by John H. Poynting in

1884. In its differential form, illustrating it as a conservation law, Poynting's theorem can be written as

$$\frac{\partial W}{\partial t} + \nabla \cdot \vec{S} + \vec{j} \cdot \vec{E} = 0, \tag{1}$$

where $\vec{S} = (\vec{E} \times \vec{B})/\mu_0$ is Poynting's flux vector and $W = (B^2/2\mu_0) + (\varepsilon_0 E^2/2)$ is the EM energy density for the magnetic and electric fields. In this equation j represents the current density in A/m^2, E is the electric field in V/m, B is the magnetic field in Tesla, and ε_0 and μ_0 are the permittivity, F/m, and permeability, henry/m, of free space, respectively. Three terms account for the conservation of EM energy within a given volume: (1) the time rate of change of EM energy density; (2) the divergence of the Poynting flux vector; and (3) the conversion of EM energy either from or to other forms of energy, often called the EM energy transfer rate. The theorem applies to all types of EM interactions from EM waves to static fields. A few descriptions of its application to space research are provided by Hill (1983), Kelley et al. (1991), and Cowley (1991). For a sufficiently long-term average, the explicit time derivative vanishes, and we have the familiar result that the conversion of EM energy to other forms is equal to the local convergence of the Poynting flux vector.

In accordance with our discussion of flux convergence, we see that Poynting's theorem specifies not the energy flux vector but only its divergence. Thus, any divergence-free vector can be added to the Poynting flux vector without contradicting Poynting's theorem. Again, as in all other sources of flux, the physically significant contribution comes when there is a divergence or convergence in the flux vector.

The other profound strength of Poynting's theorem is that it links Maxwell's equations with the fundamental laws of energy, momentum, and continuity. This proves to be extremely useful in studies regarding M–I coupling at high latitudes. The most straightforward way to illustrate this point is to use the magnetohydrodynamic (MHD) equations, also known as the center of mass equations, to describe the macroscopic behavior of the gas. The description of these equations depends on the reference frame used in defining the velocity moments of the distribution function. In Appendix A we discuss the difference between the MHD approach and the individual species approach in describing the transport equations, with an emphasis on the energy equation. More complete descriptions and discussions concerning the aeronomic transport equations can be found in the seminal work by Grad (1958), Chapman and Cowling (1970), Banks and Kockarts (1973), and Schunk (1975, 1977).

In MHD, the gas mixture is defined with respect to the center of mass velocity V defined as

$$\vec{V} = \sum_{\alpha} \frac{n_\alpha m_\alpha \langle \vec{V}_\alpha \rangle}{n_\alpha m_\alpha}, \tag{2}$$

where $\langle \vec{V}_\alpha \rangle$ is the average velocity of species α (Schunk, 1975). Applied to the thermosphere and ionosphere where the neutral mass density far exceeds the plasma mass density, the center of mass velocity is, to a very good approximation, equal to the neutral wind velocity. The link to Poynting's theorem is most easily seen when we express the MHD energy equation, as applied to the IT system, in the form

$$\vec{j} \cdot \vec{E} = \rho \frac{\mathrm{D}}{\mathrm{D}t}\left(U + \frac{V^2}{2}\right) + \nabla \cdot (\bar{\bar{P}} \cdot \vec{V}) + \nabla \cdot \vec{q}_T - \rho \vec{V} \cdot \vec{g} - \rho Q. \tag{3}$$

This expression equates the EM energy transfer rate to the time rate of change in the internal energy U, and the KE (directed motion) of the gas; the divergence in the momentum flux term, where $\bar{\bar{P}}$ is the pressure tensor; the divergence in the heat flux vector q_T; the work done on the gas by gravity g; and the radiative and chemical energy deposition term Q. A more complete description of this equation can be found in Richmond (1983). The EM energy transfer rate term couples the energy equation to Poynting's theorem, and therefore elucidates how the divergence in the Poynting flux affects the internal and KE of the neutral gas. Furthermore, it can be shown through manipulation of the MHD momentum and energy equations that the Joule heating rate accounts for that portion of the EM energy flux contributing to increasing the internal energy of the gas, that is, temperature, while the other portion of EM energy flux is expended on changing the directed KE of the gas through work done by electrodynamic forces. A straightforward approach to illustrate the partitioning is to perform a nonrelativistic transformation (a Galilean transformation) of the EM energy transfer rate from the inertial reference frame to one moving at the center of mass velocity, that is, the neutral wind, assuming that neutral wind accelerations are negligible. The current is invariant to a Galilean transformation but the electric field in the reference frame of the center of mass velocity is $\vec{E}' = \vec{E} + \vec{V}_n \times \vec{B}$, where V_n is the neutral wind velocity. The EM energy transfer rate becomes (Thayer and Vickrey, 1992)

$$\vec{j} \cdot \vec{E} = \vec{j} \cdot \vec{E}' + \vec{V}_n \cdot \vec{j} \times \vec{B}, \tag{4}$$

where the first term is the familiar Joule heating rate and the second term is the work done by mechanical forces, or the mechanical energy transfer rate. Expressed in this reference frame, the EM energy flux can be clearly partitioned into terms that have physical meaning and impact the IT system in different ways (see Thayer et al., 1995; Lu et al., 1995). A discussion of the Joule heating rate as it pertains to frictional heating is provided in Appendix A.

4. Convergence of Poynting's flux

In integral form, Poynting's theorem in steady state is

$$\int_A \vec{S} \cdot \hat{n}\, \mathrm{d}a = -\int_V \vec{J} \cdot \vec{E}\, \mathrm{d}V, \tag{5}$$

where the convergence of Poynting's flux within the volume has now been replaced by the surface integral of the

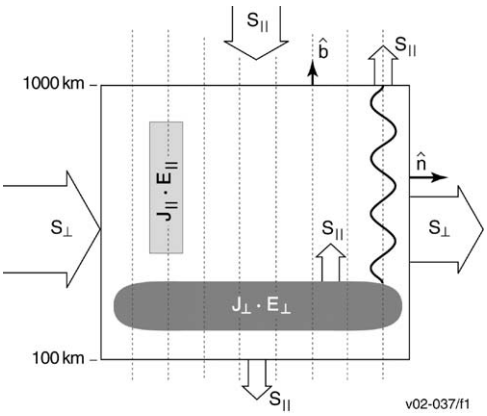

Fig. 3. Volume depiction of the Poynting flux entering and exiting the polar IT system and transferring its energy to other forms, as indicated by the shaded regions (see text for details).

Poynting vector in the direction of the unit normal vector using Gauss' Law. Fig. 3 illustrates this representation by describing a volume aligned with vertical magnetic field lines, where electric and magnetic fields, of various scale and orientation, result in Poynting flux vectors directed into and out of the volume. This representation can be used throughout the magnetosphere and ionosphere to evaluate the flow and conversion of EM energy within specific volumes. In applying this theorem to energy deposition in the IT system, the volume integral of Poynting's theorem extends from the top of the upper ionosphere, say 1000 km, to the base of the ionosphere over a unit area. Evaluated at each of the four surfaces, the top surface has a field-aligned component of the Poynting vector directed along the magnetic field and antiparallel to the unit vector b. Very little of this energy passes through the base of the ionosphere, and, at large scales, most of this flux converges in the E region and is converted to heat and momentum. Poynting flux directed out of the top of the volume may occur through the generation of EM energy by the neutral wind dynamo process. There is also a large Poynting vector perpendicular to the magnetic field, or parallel to the unit vector n, entering and exiting the side surfaces of the volume. The majority of this flux is divergence free, being produced by the conservative magnetospherically imposed electric field and the background magnetic field. However, some convergence or divergence may occur, due, for example, to field-aligned perturbation magnetic fields produced on the edges of electrojet currents.

At small scales, typically less than 10 km and/or time scales less than 1 min, the Poynting flux may reflect off the ionosphere and be redirected out of the volume producing little local dissipation (i.e., Alfvén waves) or the Poynting flux may be dissipated at higher latitudes along the magnetic field line. At these scales, the field-aligned conductivity must be considered (e.g., Farley, 1959; Boström, 1976; Heelis and Vickrey, 1991). Boström (1976) modeled this increase in parallel impedance, and the concomitant attenuation of the electric field, as a function of spatial and temporal scale size. Heelis and Vickrey (1991) investigated the dissipation of EM energy at these small scales. Field-aligned electric fields are associated with the attenuation of the magnetospheric potential, determined by the scale size of the electric field and the Pedersen to direct conductivity ratio. The total energy dissipation and its distribution, at these small scales, becomes very dependent on these mapping properties and can lead to energy dissipation at higher altitudes along the magnetic field.

It is also important to understand that not all variability in the ionospheric electric field is simply imposed by the magnetosphere. For example, small-scale intense electric fields are known to exist in the vicinity of auroral arcs (e.g., Marklund, 1984) and have even been observed to follow individual arc elements (Lanchester et al., 1996). Such fields must be associated with polarization charges set up through intense field-aligned currents. Other processes in the highly dynamic polar ionosphere can lead to electric field structuring on even smaller scales (e.g., Heppner, 1977; Sugiura et al., 1982; Ganguli et al., 1994). Such electric field patterns, when embedded in larger-scale regions of downward Poynting flux, will affect the rate of EM energy dissipation (e.g., Codrescu et al., 2000) and may in fact affect the magnetospheric source itself (Lysak and Song, 2002). Some observational evidence for this is discussed in Section 6.

If it is assumed that all the Poynting flux is being dissipated below a spacecraft measurement of the field-aligned Poynting vector, with no horizontal divergence in Poynting flux and no time-dependent changes in EM energy density (such as those due to Alfvén waves), and the measurement is below the acceleration region of the magnetosphere, then this measurement represents the net EM energy flux being dissipated in the IT system. This was the basic premise that Knudsen (1990), Kelley et al. (1991), and, later, Gary et al. (1994, 1995) used to evaluate the so-called DC Poynting flux from the HILAT and DE-2 spacecraft measurements of the horizontal electric field and magnetic field perturbations. The outcome of these studies demonstrated the utility of applying this approach to the IT system.

4.1. Altitude distribution of Poynting flux convergence

The altitude distribution of the convergence of Poynting's flux in the IT system can be related to the vertical profile in the EM energy transfer rate, $\vec{j} \cdot \vec{E}$, in units of energy density, typically $\mu W/m^3$, if we assume quasi-static fields, as stated in Eq. (5). This has been accomplished through incoherent scatter radar measurements (e.g., Brekke and Rino, 1978; Thayer, 1998a, b, 2000; Fujii et al., 1998, 1999). Further approximations have been made to estimate this quantity by assuming no neutral winds, reducing the energy transfer rate to $\sigma_p E^2$, and assuming all of its energy is deposited as heat (as was done in generating Fig. 2). Fig. 4 illustrates an altitude comparison between $\vec{j} \cdot \vec{E}$ and $\sigma_p E^2$

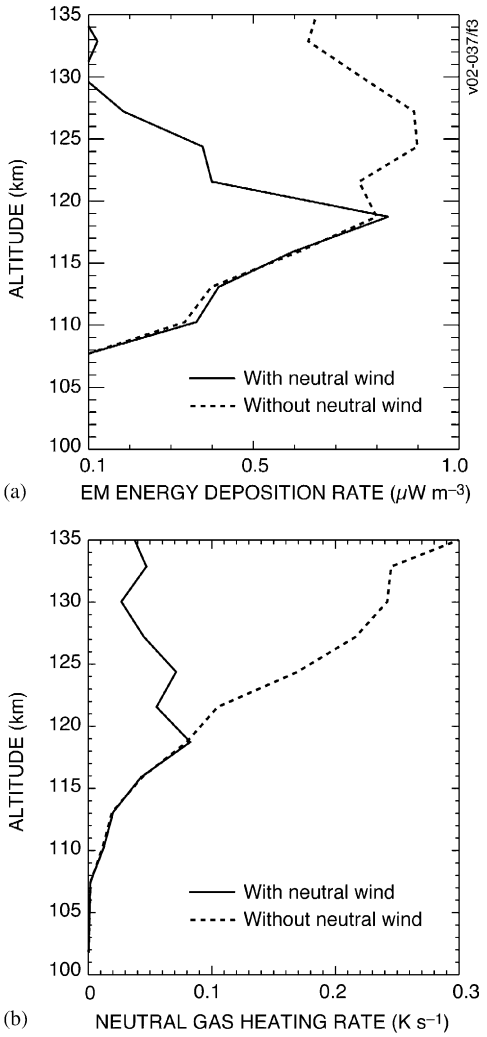

Fig. 4. Ground-based radar measurements of (a) E-region electromagnetic energy deposition rate, with neutral winds (solid line) and without (dashed line); and (b) neutral gas heating rates derived from curves presented in graph a.

estimates of the EM energy flux as measured by the Sondrestrom incoherent scatter radar. The neutral wind is implicitly accounted for by measuring the current density directly when evaluating $\vec{j} \cdot \vec{E}$; see Thayer (1998a, 2000). Clearly, the effect of wind is structured with height, with little influence on deposition rates below 120 km. However, above 120 km the two estimates are significantly different, with the winds acting to reduce the amount of energy deposited by significantly impacting the current magnitude and direction with respect to the electric field.

The heating rate in Kelvins per second is given in Fig. 4b for the EM energy transfer rates shown in Fig. 4a, assuming that all the EM energy flux is converted to heat. It is clear that the heating of the neutral gas in the topside E region is a factor of 3 smaller, due to the effects of the neutral wind on the current. Thus, the wind behavior, with height and time, plays a critical role in determining energy deposition and subsequent heating. This has been inferred from results published by Thayer (1998a, b, 2000) and Fujii et al. (1998, 1999). Recent wind observations from the WINDII instrument on UARS also illustrate strong topside E-region wind behavior at high latitudes, in excess of 400 m/s, during active times (Zhang and Shepherd, 2002).

Whether all or only a portion of the Poynting flux converging in the E region is converted to heat is critical to understanding the global IT system response to this energy source. Thayer and Vickrey (1992) demonstrated that the Poynting flux is partitioned between Joule heat and mechanical energy with thermospheric winds playing a key role. Lu et al. (1995) used the IT general circulation model (inherently large scale) to assess the partitioning of Poynting flux, and found that almost all of the energy, after integrating over the hemisphere, is converted into Joule heating (94%), with the remainder going into mechanical energy of the neutral gas. However, locally the partitioning to Joule heat can be less depending on the localized neutral wind field (Thayer et al., 1995).

It has been shown, for example, by Mayr and Harris (1978; see also the references cited), that changes in temperature, composition, and wind are dramatically different when driven by a heat source as compared to a momentum source. Given an external heat source such as Joule heating, the temperature increase produces a pressure field that leads to divergent wind flow. This divergent wind flow is very efficient in creating composition changes. A momentum source, such as that imposed at high latitudes by ionospheric convection, produces weak divergent wind flow and consequently little temperature and composition change. In their model simulations, Mayr and Harris (1978) found the momentum source of ionospheric convection to be more than 20 times less effective for density variations and 100 times less effective for temperature changes than when Joule heating is considered as the source. Moreover, Joule heating causes an increase in the temperature and density of heavier atmospheric constituents such as molecular nitrogen and oxygen, as well as a decrease in density of the lighter constituents such as atomic oxygen and helium. The momentum source resulted in small temperature and composition changes that were basically in phase with each other.

The scale size of the Poynting flux and its partitioning to heat and momentum are also important, as theoretical investigations of the thermospheric response to high-latitude heat and momentum sources have indicated a dependence on the scale size of the source (Mayr and Harris, 1978). Larsen and Mikkelsen (1983), who applied the theory of geostrophic adjustment to support the numerical results of Mayr and Harris, found that the response of the divergent wind field increases as the scale size of the forcing increases. Meanwhile, the response of the rotational wind component

becomes greater as the scale size of the forcing decreases. The scale sizes are related to the Rossby radius of deformation, a fundamental horizontal length scale in atmospheric dynamics over which the mass and momentum fields adjust to forces of specific size. Larsen and Mikkelsen (1983) have shown the Rossby radius of deformation to vary from greater than 600 km in the E region to 200 km in the F region. For forces exceeding the radius of deformation, the mass field adjusts and the wind field follows in response to the change in pressure. In other words, as the scale size of Joule heating increases the thermosphere responds by producing significant changes in composition and stronger divergent wind fields. On scale sizes smaller than the Rossby radius, the Lorentz force becomes more efficient in generating a rotational wind field, with the mass adjusting accordingly. Thus, we must be careful and remind ourselves that the source of Poynting flux is a spectrum of temporal and spatial scales that may be processed differently by the neutral gas.

5. KE flux into the polar IT system

The polar regions of the Earth are subject to constant bombardment by charged particles covering a broad spectrum of energies. These particles dissipate their KE through a series of collisions that ionize, excite, and heat the atmospheric gases and produce the optical aurora. In the polar cap, the particle flux may originate on open field lines, producing cusp aurora and polar cap arcs. Within the auroral oval there exists a continuous flux of hot thermal electrons and protons resulting from pitch angle diffusion of plasma sheet particles into the ionospheric loss cone, producing the diffuse aurora. The most energetic and intense fluxes, however, are carried by electrons that have been accelerated to thousands of electron volts along their trajectory from the magnetosphere to the ionosphere. This acceleration process produces the discrete aurora. The downward KE flux in the discrete aurora can exceed the downward Poynting flux locally (as shown in Fig. 2). Its convergence in the IT system is the primary focus of this section.

First, let us precisely define KE flux in the auroral context. Measurements of the auroral acceleration region (AAR) have shown that it is well approximated by an electrostatic potential drop. A potential drop ϕ imposed on a collisionless neutral plasma will accelerate charged particles to average drift velocity $|v| = \sqrt{2e\phi/m}$ (assuming $e\phi \gg kT$). The net KE flux (W/m^2) carried by the accelerated beam is $\vec{K} = \rho(|v|^2/2) \cdot \mathbf{v}$, where ρ is the particle mass density. The KE flux in the electron beam will exceed that of the oppositely directed ion beam by a factor of $\sqrt{m_i/m_e}$ (equal to 42 for a proton plasma). Thus, electrons carry $> 97\%$ of the total KE flux produced in the AAR.

The number flux of electrons produced by the imposed electrostatic potential drop will exceed that of the ions by the factor v_e/v_i, which is also equal to $\sqrt{m_i/m_e}$. Thus, electrons also carry most of the electric current in the AAR. This means that a measurement of the net number flux of downgoing accelerated electrons below the AAR provides a good estimate of the upward field-aligned current carried within an auroral arc (e.g., Evans et al., 1977; Lyons et al., 1979).

5.1. Convergence of KE flux

As stated earlier, KE flux and Poynting's flux are dissipated in fundamentally different ways in the IT system. While both fluxes heat the neutral gas, KE flux also ionizes and excites the gas. The ionizing reactions alter the ionospheric conductivity which, in turn, may influence the future partitioning between Poynting's flux and KE flux. It is, therefore, critical to understand precisely how and at what altitude auroral KE flux is dissipated.

Let us consider a single electron with velocity v impinging the top of the atmosphere. This primary electron suffers a series of elastic and inelastic collisions, producing numerous secondary electrons and eventually thermalizing to the ambient ionospheric plasma. First-principle models of the electron transport and degradation process have been presented by several authors (e.g., Strickland et al., 1989; Lummerzheim and Lilensten, 1994). For the present discussion, however, we wish to determine the partitioning of the incident KE among the processes of ionization, excitation, and heating.

Following Dalgarno (1962), we define the average energy deposited per ion–electron pair produced,

$$W_{\text{ion}} \equiv E/N_{\text{T}}(E), \tag{6}$$

where $N_{\text{T}}(E)$ is the total number of ion–electron pairs of any type produced by the absorption of an electron with initial energy E into the atmosphere. It so happens that for a given substance, W_{ion} is largely independent of the mass, charge, or velocity of the impinging particle. This effect can be accounted for theoretically. A more remarkable fact is that W_{ion} is also relatively insensitive to the ionizing potential, regardless of whether the substance is gas, liquid, or solid. This observational result has no general theoretical explanation, but the reader is encouraged to read Fano (1946) for a detailed semi-quantitative discussion.

Dalgarno (1962) has summarized W_{ion} for a variety of gases: for N_2, $W_{\text{ion}} = 37$ eV; for O_2, $W_{\text{ion}} = 33$ eV; for O the appropriate measurement has not been made, but we may assume it has about the same value as the other major atmospheric species. Using a typical air mixture at 100 km, $W_{\text{ion}} = 36$ eV; at 200 km, $W_{\text{ion}} = 35$ eV. A value of $W_{\text{ion}} = 35.5$ eV is reasonable for the 80–200 km altitude range, where the majority of auroral energy is dissipated.

Note that W_{ion} exceeds the ionizing potential of each species by about a factor of two. A quantitative estimate of this ionization efficiency may be computed from a weighted average of ionization-excitation potentials for the dominant atmospheric species in the 80–200 km altitude range. Assuming the atmosphere comprises O, N_2, and O_2,

the ionization efficiency is given by

$$\gamma_{\text{ion}} = \frac{N_{\text{O}} \sum_i b_i w_i + N_{\text{O}_2} \sum_j b_j w_j + N_{\text{N}_2} \sum_k b_k w_k}{W_{\text{ion}}(N_{\text{O}} + N_{\text{O}_2} + N_{\text{N}_2})}, \qquad (7)$$

where N refers to the species number density, b is the branching ratio, and w is the ionization potential. The summations are over all the allowable excited states achieved in the ionizing reaction. The relevant branching ratios and ionizing potential are given in Table A4.1 by Rees (1989). Using the atmospheric densities at 150 km derived from MSIS for the conditions applied in Fig. 2, Eq. (7) gives an ionization efficiency of ~45%.

Since excited states are produced in both ionizing and nonionizing reactions, it is not possible to explicitly distinguish the excitation efficiency from the ionization efficiency. However, if we take the average excitation potential to be ~2 eV, then the excitation efficiency should be ~5%.

The remaining "wasted" energy is deposited as heat in the neutral gas (a small amount is also lost in molecular dissociation reactions, which produce no local heating). Rees et al. (1983) have studied the neutral gas heating efficiency for auroral precipitation. Below 200 km they estimated the heating efficiency to be ~50%; above 200 km the heating efficiency drops off in a roughly linear fashion to ~5% at 400 km.

In summary, the partitioning of auroral KE flux in the 80–200 km altitude range is roughly 50% heating, 45% ionization, and 5% optical production.

5.2. Auroral ionization

We now consider the distribution of ion production along the auroral flux tube threading the polar atmosphere. The invariance of W_{ion} with composition and incident energy means that the shape of the energy deposition curve depends only on the altitude distribution of mass density in the atmosphere (e.g., Rees, 1963; Vallance-Jones, 1974; Rees, 1989). Rees (1963) used this fact, along with laboratory measurements of electron absorption in air, to develop a method for computing the energy deposition function for an arbitrary incident electron beam. A computation of this type is shown in Fig. 5. Fig. 5a gives three curves of energy versus differential number flux. These spectra were measured by the ESA instrument on the FAST satellite as it approached the poleward boundary of an active auroral oval. The dashed curve is a typical "bump on tail" distribution associated with visible discrete aurora. The solid curve has a lower characteristic energy but higher number flux. The lowest energy curve is typical of the intense field-aligned distributions often observed on recently reconnected field lines at the nightside polar cap boundary.

Fig. 5b gives the corresponding ion production profiles for these representative spectra, computed with the MSIS neutral atmosphere model for moderately active conditions at Sondrestrom in winter, and the unidirectional energy distribution function computed by Rees (1963). The upper abscissa gives the energy deposition rate derived by dividing the lower abscissa by 35.5 eV and converting to $\mu W/m^3$.

Once the ion production profile is defined, the time-dependent response of ionospheric density can be computed from an appropriate continuity calculation. At altitudes below 200 km, ionospheric continuity can be approximated by the expression

$$\frac{dN_e(z)}{dt} = P(z) - \alpha(z) N_e^2(z), \qquad (8)$$

where P is the ion production rate, and α is the effective recombination coefficient. Fig. 5c gives the ionospheric response computed with the expression for α given by Vickrey et al. (1982). The simulations start with a uniform initial

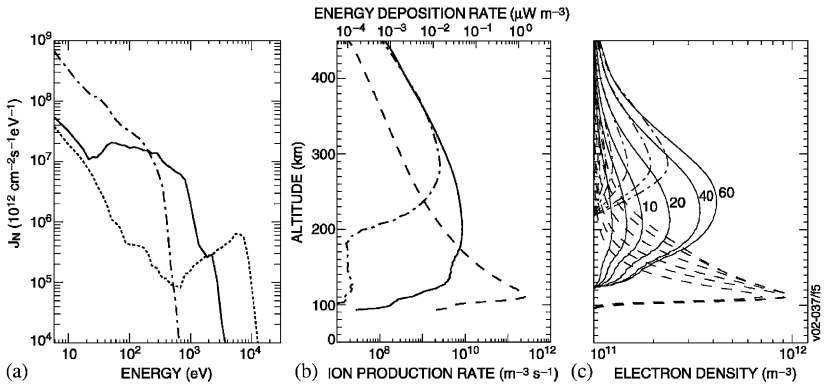

Fig. 5. (a) Three examples of downward differential number flux spectra near the polar cap boundary during substorm recovery, measured by the FAST satellite. (b) Corresponding ion production rate profiles computed from laboratory measurements of electron penetration in air (Rees, 1963): ion production rate is shown on the lower abscissa, and the energy deposition rate is shown on the upper abscissa. (c) Corresponding ionospheric density at $t = +3$, 6, 10, 20, 40, and 60 s, computed numerically from Eq. (8).

density of 1×10^{10} m^{-3}, and profiles are shown at $t = 3$, 6, 10, 20, 40, and 60 s. For the highest energy distribution (dashed line), the peak density occurs at $\sim$ 110 km and steady state is reached within $\sim$5 s. The other distributions do not reach steady state in the 60 s time period shown, but do demonstrate that a significant enhancement in F-region density can be created by auroral precipitation, provided the auroral source remains stationary for tens of seconds. For instance, for the solid profile the density increases by a factor of 2 within $\sim$15 s; for the dashed-dot profile a factor 2 increase requires nearly 1 min.

We note that although Eq. (8) is not appropriate for the F-region in general, it is a valid model for the 1 min time duration shown. The mean lifetime of an ion above 180 km is $>$ 60 s (Chamberlain and Hunten, 1987). This is longer than the entire simulation time shown in Fig. 5c. For this period, the right-hand side of Eq. (8) is dominated by P. For longer periods, however, one must consider atom–ion interchange reactions (i.e., so-called β chemistry).

Fig. 5 suggests that there should, in general, be an observable time lag between auroral luminosity and the ionospheric density response. This lag can be quantified using simultaneous optical and radar measurements in the magnetic zenith. Fig. 6 compares the luminosity of the N_2 first positive group (1PG) in the magnetic zenith, with $\int_0^\infty \alpha N^2 \, \partial z$, computed from incoherent scatter radar (ISR) measurements at 1 s intervals (Semeter and Doe, 2002). For this auroral surge event, most of the KE was deposited below 150 km, where N_2 is the dominant neutral species. As such, the N_2 1PG brightness is a reasonable proxy for the ion production rate. The discrepancy between the two estimates is most extreme when either the background density is low ($<$ 02 : 28 : 00 UT) or when the source is highly variable (e.g., 02:28:15 UT). In general, however, the curves track reasonably well. This implies that for hard precipitation, ISR measurements can be used to compute the altitude profile of ion production

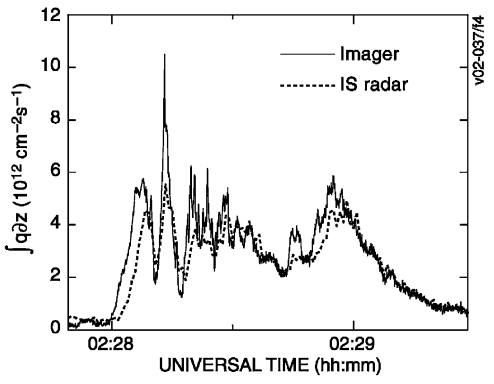

Fig. 6. Height-integrated ion production rate computed optically (solid line) and using ISR measurements of electron density (dashed line), illustrating the time lag of the ionospheric response to an auroral source.

rate and, hence, auroral energy deposition rate:

$$\varepsilon(z) = W_{\text{ion}} \alpha(z) N_e^2(z). \tag{9}$$

Eq. (9) prescribes how one goes "backward" from Fig. 5c to b. In some cases, the incident electron spectrum (Fig. 5a) may also be recovered using eigen decomposition techniques (Brekke and Hall, 1989), although the solution is often not unique.

Finally, we note that the above discussion pertains only to electrons whose energy exceeds $\sim$70 eV. At lower energies, electron trajectories are significantly perturbed in the ionizing collisions (see the experimental results of Barrett and Hays, 1976). The net effect is that low-energy electron beams deposit their energy preferentially at higher altitudes than predicted by the method of Rees (1963). This suggests that soft precipitation may be a more important source of F-region ionization than is commonly believed.

6. Interaction between Poynting and KE fluxes

The separate treatments of Poynting flux and KE flux in the previous sections follows, in a broad sense, the general approach in the literature, where papers discuss Joule heating and particle heating as separate sources of energy with different influences on the IT system. However, these sources are intimately linked in the magnetosphere and dependent on the state of the IT system. Hence, the preconditioning of the thermosphere and ionosphere (set up by the convergence of other sources of flux, like solar irradiance), the change in the IT state after the interaction with magnetospheric fluxes, and the electrodynamic connection between the IT system and the magnetosphere, can act to change the amount and possibly the type of flux being provided by the magnetosphere. Indeed, an entire class of auroral models is based on feedback between Poynting's flux and KE flux (Atkinson, 1970; Sato, 1978; Lysak and Song, 2002). In this section we review observational evidence related to mutual interactions between Poynting's flux and KE flux.

Under the so-called perfect MI coupling, KE flux is negligible and the field-aligned current has exactly that magnitude required to dissipate the Poynting flux delivered by the magnetospheric generator to the IT system. However, there is a limit to the magnitude of the field-aligned current that can be carried by the magnetospheric plasma (computed theoretically by Knight, 1973). When this limit is exceeded, a field-aligned potential drop of tens of kiloelectronvolts can appear at an altitude of 1.5 to 3 Re.

In this work we are not concerned with the physics governing the formation of the AAR, but rather with its bulk characteristics in terms of convergence and divergence of energy. A simple expression linking the two magnetospheric energy fluxes can be derived as follows. If we assume that the only force on the magnetospheric plasma is the Lorentz force, the ion and electron momentum equations

take the general form

$$\frac{m\mathrm{D}\vec{V}}{\mathrm{D}t} = q[\vec{E} + \vec{V} \times \vec{B}]. \tag{10}$$

Multiplying both sides by velocity and plasma number density leads to the KE equation

$$\frac{\mathrm{D}}{\mathrm{D}t}\left(\frac{\rho|\vec{V}|^2}{2}\right) = qN_e\vec{V} \cdot \vec{E} = \vec{j} \cdot \vec{E}. \tag{11}$$

Expanding the total derivative and assuming the plasma is incompressible, that is, $\vec{\nabla} \cdot \vec{V} = 0$, results in the expression

$$\frac{\partial}{\partial t}\left(\frac{\rho|\vec{V}|^2}{2}\right) + \nabla \cdot \left(\frac{\vec{V}\rho|\vec{V}|^2}{2}\right) = \vec{j} \cdot \vec{E}. \tag{12}$$

Substituting for $\vec{j} \cdot \vec{E}$ in Eq. (1) produces the conservation equation

$$\frac{\partial(W + M)}{\partial t} + \nabla \cdot (\vec{S} + \vec{K}) = 0, \tag{13}$$

where M is the KE density of the plasma and $\vec{K}$ is the KE flux vector. This equation demonstrates the interplay between the plasma and the fields and can be used to provide a general description of the magnetosphere (Hill, 1983). In essence, regions where the KE of the plasma is increasing come at the expense of the energy contained in the EM fields. In steady state, a divergence in KE flux must always be accompanied by a convergence in Poynting flux; and an electric field and current must be present wherever this energy transfer is taking place. Observations have demonstrated that such an adiabatic exchange of energy between fields and particles is in fact a good approximation for the AAR (McFadden et al., 1999).

Keiling et al. (2002) used POLAR spacecraft measurements to compare the downward Poynting flux carried by Alfvén waves at 4–6 Re (above the AAR) with KE flux derived from auroral luminosity at the satellite footprint. The 40 events they studied showed good correlation between the Alfvénic Poynting flux and auroral KE flux, thus supporting the adiabatic energy conversion hypothesis. The range of Poynting's flux magnitudes was between 0.01 and 1.0 mW/m^2, which corresponds to 1.25–125 mW/m^2 when mapped to the ionosphere. These limits are in the normal to extreme range of the Poynting flux values observed by ground-based radars (e.g., Thayer, 2000). The radar technique has spatial resolution of $\sim$ 100 km and temporal resolution of $\sim$ 5 min, suggesting that the E and δB perturbations are associated with large-scale convection patterns and large-scale currents, respectively (often referred to as the DC Poynting flux). POLAR estimates of the Poynting flux are associated with small-scale perturbations in E and B related to Alfvén waves. Collectively, the observations suggest that DC Poynting flux is mapped to the ionosphere unimpeded, while the Alfvénic Poynting flux converges in the AAR, leading to a divergence in KE flux and the acceleration of auroral electrons as implied by Eq. (13).

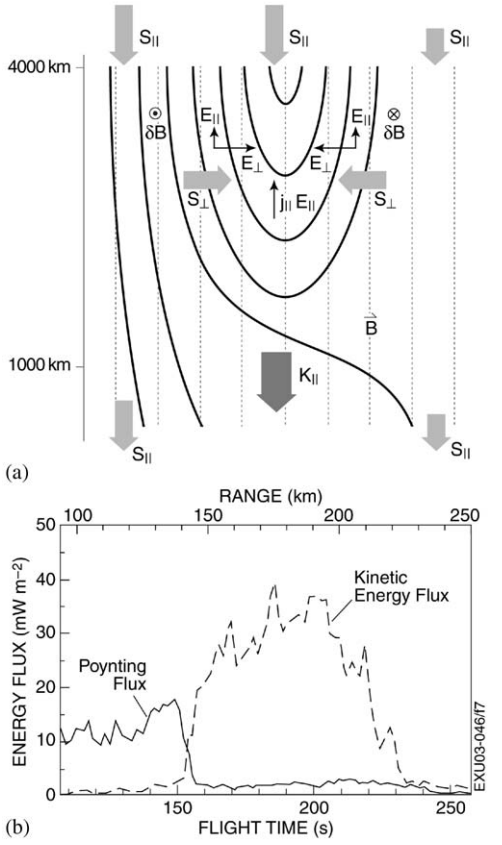

Fig. 7. (a) Schematic illustration of electromagnetic energy conversion in the AAR, consistent with satellite and ground-based measurements of discrete aurora in the pre-midnight sector. (b) Rocket measurements of Poynting flux and kinetic energy flux across an arc boundary below the acceleration region (Evans et al., 1977).

The generation of parallel electric fields by the Alfvén waves has for some time been a suggested acceleration mechanism of auroral electrons (e.g., by Hasegawa, 1976).

Fig. 7a presents a model for adiabatic energy conversion in the AAR, similar to that presented by Mozer et al. (1980). The potential contours are qualitatively consistent with satellite and ground-based measurements of discrete aurora in the pre-midnight sector. Above the AAR, magnetospheric energy is transported as downgoing Poynting flux. The flux is strongest near the equatorward edge of the AAR (the upstream side of the convection electric field), where an enhancement in Joule dissipation is often observed in the ionosphere (Marklund, 1984). Within the AAR there exists a negative $\vec{j} \cdot \vec{E}$ whose magnitude is equal to the conversion rate of Poynting flux to KE flux. The existence of a parallel electric field, in both the upward and downward current regions, is now an established experimental fact (e.g., Mozer and Hull, 2001; Ergun et al., 2001). As a result, electrons and ions are accelerated, yielding a vertical gradient in KE

flux that balances the local convergence of Poynting flux within the volume. The upward current induces a perturbation magnetic field and hence a perpendicular component to the Poynting vector, $\vec{S}_\perp = \vec{E}_\parallel \times \delta\vec{B}_\perp$. In a U-shaped potential pattern $\vec{S}_\perp$ converges toward the center. This convergence is required because $\vec{K}_\parallel$ maximizes at a point where $\vec{E}_\perp$ (hence $\vec{S}_\parallel$) goes to 0. In an S-shaped potential pattern there will also be an $\vec{S}_\perp$, but it need not be convergent.

Fig. 7b shows an ionospheric measurement below the acceleration region that is consistent with this model. The plot shows Poynting flux and electron KE flux derived by Evans et al. (1977) from sounding rocket measurements across an auroral arc boundary. An enhancement in Poynting flux is observed near the equatorward edge of the arc. As the rocket traverses the arc boundary, there is a smooth transition from Poynting flux $\vec{S}$ to KE flux $\vec{K}$, with no abrupt change in the net energy, $\vec{S} + \vec{K}$. Recent measurements from POLAR (Mozer and Hull, 2001) and FAST (Ergun et al., 2001) suggest that such U-shaped potentials are likely embedded within larger-scale regions of $\vec{S}_\parallel$. If this is true, then the increase in $\vec{K}$ represents a "bite out of" the large-scale region of $\vec{S}$, and the strict anticorrelation in Fig. 7b projects the efficient field-aligned energy conversion process suggested by Eq. (11). Patterns such as this have been observed in other rocket experiments (e.g., those of Primdahl and Sandahl, 1987; Kletzing et al., 1996).

Fig. 8 presents another way of observing the relative interplay between the Poynting flux and KE flux, this time using ground-based ionospheric measurements. The plot shows ISR measurements recorded from a fixed position looking up the magnetic field line during the formation of an auroral arc. The ion temperature is directly proportional to the square of the electric field in the neutral reference frame (see Appendix A); the electron density enhancement at 111 km is caused by precipitating electrons, and can be related to the local energy deposition rate by Eq. (9). These measurements provide reasonable proxies for simultaneously monitoring changes

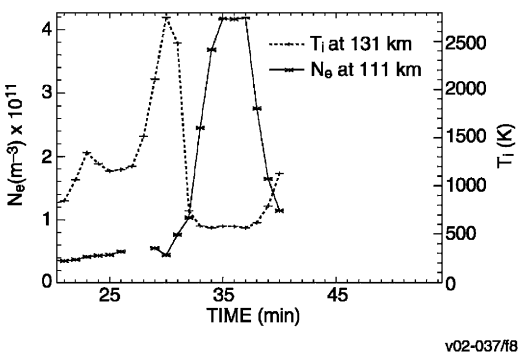

Fig. 8. Sondrestrom IS radar measurements of ion temperature (T_i) and electron density (N_e) recorded during the formation of an auroral arc in the magnetic zenith.

in the Poynting flux and KE flux via ground-based radar. The anticorrelation between Ti and Ne is the ionospheric manifestation of an energy conversion boundary (temporal in this case) similar to the one presented in Fig. 7b. The time resolution of the measurement is 5 min in this case, but new ISR modes are increasing that time resolution to 1 min or less (e.g., Semeter and Doe, 2002). Similar anticorrelations have been observed using radar measurements of the full electric field vector (e.g., see Vickrey et al., 1982; Robinson, 1984; Sugino et al., 2002). However, there are also times when electric fields and conductances are not anticorrelated (e.g., see Marklund, 1984), and the model presented in Fig. 7a may not always be applicable.

This relationship between fluxes can also be investigated using measurements from a satellite in a high-inclination, low-altitude (<1000 km) orbit. Newell et al. (2001), for instance, have compiled a statistical study of KE flux entering the topside ionosphere for a complete solar cycle. Their results illustrate a large difference between the frequency of intense aurora in sunlight and in darkness, and a slightly lower occurrence rate of intense aurora at solar maximum than minimum. These results suggest that the state of the ionosphere, presumably due to changes in the solar VUV irradiance, has an impact on the mechanisms responsible for auroral acceleration. It is unclear whether the impact on the AAR is due to the difference in ionospheric conductance or due to a difference in the amount of plasma available within the AAR, but the evidence for some form of mutual interaction between the ionospheric state and the magnetospheric source is strong.

A less publicized statistical study involved the direct satellite monitoring of field-aligned Poynting flux entering the ionosphere. Gary et al. (1995) used 576 orbits over the 2-year lifetime of the Dynamics Explorer-2 spacecraft to estimate the field-aligned Poynting flux. They found that dayside values of the Poynting flux directed into the ionosphere were 20–50% higher than nightside values. This result, combined with the Newell et al. (2001) results, is suggestive of a large-scale anticorrelation in Poynting flux and KE flux. However, very few ionospheric satellite studies have directly measured and contrasted the two energy fluxes. One such unique satellite study was that of Kelley et al. (1991), whose Fig. 5 also indicates an anticorrelation in the two fluxes. The anticorrelation in fluxes supports the general idea that Poynting flux is the energy source for the generation of aurorally accelerated electrons that is manifested in the ionosphere as KE flux.

7. Summary

This paper has discussed the convergence of energy flux in the transition region, the 80–200 km altitude range, of the polar atmosphere, with an emphasis on magnetospheric electromagnetic and kinetic energy fluxes. From an aeronomic perspective, the convergence of flux drives the physics and

chemistry of the polar ionosphere and thermosphere system. From a magnetospheric perspective, this thin transition region, from collisionless to collision dominated, represents an electrodynamic boundary condition that dictates the necessary balance between plasma density and cross-field ion mobility to allow field-aligned currents to close. Understanding the physics and chemistry of this transition region and the processes that govern currents, conductivities, and fields in this domain is of central importance to MI coupling research.

We have shown that, at polar latitudes, the rate of energy deposition in the 80–200 km altitude range by magnetospheric fluxes can often exceed the rate of energy deposition by solar VUV radiation. Differences in how this energy is deposited lead to mutual interactions among the fluxes, influencing not only how and where a flux is deposited, but also the source region itself.

An important issue raised in this paper is the intimate relationship between the electromagnetic and kinetic energy fluxes. Because these sources have such different spatial and temporal behavior and impact the thermosphere and ionosphere in very different ways, it is imperative for the field of polar aeronomy that their physical interplay be understood, and their input into the high latitude regions be routinely and accurately measured. It is also a challenge to the polar aeronomic community to resolve the issue concerning the role of the upper atmosphere in modifying the flux of energy from the magnetosphere. The thermosphere (representing the neutral gas winds, composition, and temperature) continues to be a challenge in understanding its response to the various fluxes, with progress inhibited by our limited ability to adequately measure these basic neutral state parameters. This situation is further exasperated by the infrequent and, at times, indirect monitoring of magnetospheric energy flux, particularly the Poynting flux, even though it represents a primary source of energy to the high latitudes and has global implications. The continued model development and the planned advancements in ground-based and space-based observations of the IT system provide hope that these issues will ultimately be resolved.

Acknowledgements

This work was supported by National Science Foundation (NSF) Cooperative Agreement ATM-9317167 and NSF GEM grant ATM-0302672. We would like to thank Drs. Rick Doe, Craig Heinselman, and Art Richmond for many helpful discussions regarding this work.

Appendix A.

The term Joule heating rate has been expressed in many forms within the literature; here we express it as a height-resolved quantity in units of $\mu W/m^3$:

$$j \cdot E'; \ \sigma_p E'^2; \ \frac{j^2}{\sigma_c},$$

where j is the ionospheric current density, E' is the electric field in the reference frame of the neutral gas, σ_p is the Pedersen conductivity, and σ_c is the Cowling conductivity. These terms are all equivalently equal to the Joule heating rate. However, the difficulty of observing these quantities simultaneously and the necessity to determine the Joule heating rate parameter because of its significant impact on the IT system, sometimes lead to significant approximations to the above expressions. There are many and various ways of approximating the Joule heating rate, depending on the type of measurement set available, often with little means of determining the accuracy of their assumptions (e.g., de la Beaujardière et al., 1991; Rich et al., 1987, 1991; Kamide and Kroehl, 1987).

One particular approximation that has stemmed from theoretical considerations and confirmed through measurements is the frictional heating rate and its equivalence to the Joule heating rate (cf. St. Maurice and Schunk, 1981; Killeen et al., 1984). However, confusion continues to arise in discussions of these two terms. The confusion relates to the origin of the two terms and the different definitions of their reference frames. The Joule heating rate is a term in the MHD internal energy equation that accounts for the conversion of EM energy into thermal motion of the gas. It is a positive definite quantity that is often likened to Ohmic heating in a wire. The frictional heating rate is a term in the individual species description of the energy equation. It typically relates to the interaction between the relative drift velocities of ions and neutrals. It is generated from measurements of the appropriate velocity moment of the Boltzmann collision integral and then evaluation of the integral, assuming that the species distribution function is described by a Maxwellian (equivalent to a five-moment approximation: see Schunk (1975) for a more thorough discussion). Thus, the two terms have distinctly different origins: A general understanding of the MHD approach and the individual species description is required. The best approach is to study the early work on this subject, as referenced in Section 3. Here, we will provide a general distinction between the two systems.

Owing to the definition of the center of mass velocity, one can obtain the MHD system of equations from the individual species equations by summing each species' equation over all constituents. The MHD equations are based on the single fluid concept, so that all the terms in the MHD equations reflect the total description of the gas or plasma, that is, the total mass, total momentum, and total energy of the system. However, the individual species' equations contain terms that reflect the species description within the gas or plasma, which may not affect the behavior of the gas or plasma as a whole. Thus, terms in the individual species equations may cancel out when summed over all constituents. For example,

in the energy equation described by the individual species approach, the temperature is defined relative to the species' own drift velocity, so any collision will affect the internal energy of that particular species. However, in the MHD approach the collision terms vanish because they act so as to redistribute the internal energy without changing the overall energy of the gas or plasma. A way of reconciling the differences between the two systems is to consider the individual species approach as a path-dependent system that accounts for the processes between the different species that lead to macroscopic changes in the system. The MHD approach is independent of the path by which energy is transferred amongst the species in its description of the macroscopic behavior of the gas.

For example, the MHD Joule heating rate term accounts for the internal energy change in the gas due to currents that, because the MHD equation largely describes the neutral gas, ends up as heat to the neutral gas without consideration of the path. The frictional heating rate is a descriptor of the energy path to the neutral gas; that is, ions moving through the neutral gas will be heated and this thermal energy will be transferred to the neutral gas via random collisions. The following text provides the details illustrating the relationship between the frictional heating rate and the Joule heating rate.

The term frictional heating rate originates from an approximate solution to the Boltzmann collision integral. Only for the simplest case has a general collision term been evaluated that applies to arbitrary interparticle force laws, large species temperature differences, and large relative drifts between the two interacting species (cf. Schunk, 1975, 1977; St. Maurice and Schunk, 1979; Schunk and Nagy, 1980). As such, the general expression for the individual species energy equation that accounts for collisions can be written as

$$\frac{\delta E_s}{\delta t} = \sum_t \frac{n_s m_s \nu_{st}}{m_s + m_t} \left\{ \begin{array}{l} 3k_B(T_t - T_s)\Psi_{st} \\ +m_t(\vec{V}_s - \vec{V}_t)^2 \Phi_{st} \end{array} \right\}, \tag{A.1}$$

where s is the species of interest, either ion, electron or neutral, and t is the species of interaction. A list of the parameter definitions is provided in Table 1. The factors Ψ and Φ are the velocity-dependent correction terms discussed by Banks and Kockarts (1973) and Schunk (1975, 1977). For Maxwell molecule interactions (where the interaction potentials vary inversely as the fourth power of the particle separation) the collision cross-section is independent of velocity, thus setting the velocity-dependent correction factors as equal to unity. This assumption is often used in ionospheric studies (cf. Killeen et al., 1984).

The first term in Eq. (A.1) represents the heat exchange term between species, and the second term is the frictional heating term due to differential velocities between the two species. As an example, the individual energy equation describing the neutral species has a number of important terms, one of which accounts for collisions between neutrals and ions, that is,

$$\frac{\delta E_n}{\delta t} = \sum_i \frac{n_n m_n \nu_{ni}}{m_n + m_i} \left\{ \begin{array}{l} 3k_B(T_i - T_n) \\ +m_i(\vec{V}_n - \vec{V}_i)^2 \end{array} \right\} + \cdots. \tag{A.2}$$

Now, it has been shown for the ion species that its energy equation can be approximated, below about 400 km, to good degree by a balance between the energy exchange term and the frictional heating term (Schunk and Sojka, 1982; St. Maurice and Hanson, 1982, 1984; Killeen et al., 1984), such that

$$\frac{\delta E_i}{\delta t} = 0. \tag{A.3}$$

Therefore,

$$3k_B(T_i - T_n) \cong m_n(\vec{V}_i - \vec{V}_n)^2.$$

Using this assumption, we can rewrite the neutral species equation (A.2) as

$$\frac{\delta E_n}{\delta t} = \sum_i \frac{n_n m_n \nu_{ni}}{m_n + m_i} \left\{ \begin{array}{l} m_n(\vec{V}_i - \vec{V}_n)^2 \\ +m_i(\vec{V}_i - \vec{V}_n)^2 \end{array} \right\} + \cdots \tag{A.4}$$

and when the relation

$$n_n m_n \nu_{ni} = n_i m_i \nu_{in} \tag{A.5}$$

is used the equation simplifies to

$$\frac{\delta E_n}{\delta t} = \sum_i n_i m_i \nu_{in}(\vec{V}_i - \vec{V}_n)^2. \tag{A.6}$$

Table 1
Symbols

σ_c	Cowling conductivity
σ_H	Hall conductivity
σ_P	Pedersen conductivity
ν_{in}	Ion–neutral collision frequency
ν_{en}	Electron–neutral collision frequency
Ω_i	Ion gyrofrequency
Ω_e	Electron gyrofrequency
k_i	Ion mobility coefficient (Ω_i/ν_{in})
k_e	Electron mobility coefficient (Ω_e/ν_{en})
m_s	Mass of species s (i for ion, n for neutral)
n_s	Number density of species s (i for ion, n for neutral, e for electron)
q_i	Electronic charge
V_s	Vector velocity (i for ion, n for neutral, e for electron)
T_s	Temperature (i for ion, n for neutral, e for electron)
j	Current density
E	Electric field in the inertial reference frame
B	Earth's magnetic field strength
X'	A field vector in the neutral wind reference frame

Thus, using the approximated ion energy equation (A.3), we can reduce the collision term in the neutral species energy equation (A.2), to a single term that can be called the frictional heating rate. This term could have also been expressed as

$$\frac{\delta E_{\mathrm{n}}}{\delta t} = \frac{3k_{\mathrm{B}}}{m_{\mathrm{n}}} \sum_i n_i m_i \nu_{i\mathrm{n}} (T_i - T_{\mathrm{n}}) \tag{A.7}$$

if we use the approximate ion energy equation (A.3) to replace the frictional heating term with the heat exchange term. Thus, the two are interchangeable for as long as the ion energy equation approximation is valid.

To equate the Joule heating rate from the MHD equation to the frictional heating term provided above requires a few other general approximations. First, the MHD Joule heating rate can be written without approximation in terms of the individual species description as

$$\vec{j} \cdot \vec{E}' = \sum_i q_i n_i (\vec{V}_i - \vec{V}_{\mathrm{e}}) \cdot \vec{E}'. \tag{A.8}$$

Because the current is invariant to a coordinate change to the neutral gas reference frame, the Joule heating rate can be equivalently written as

$$\vec{j} \cdot \vec{E}' = \vec{j}' \cdot \vec{E}' = \sum_i q_i n_i (\vec{V}'_i - \vec{V}'_{\mathrm{e}}) \cdot \vec{E}', \tag{A.9}$$

where the primes represent variables in the neutral gas reference frame. If it is assumed that the ion and electron equations of motion perpendicular to the magnetic field line are in steady state and governed only by the Lorentz and ion drag forces, the ion and electron equations in the reference frame of the neutral gas can be written (Brekke, 1997), respectively, as

$$\vec{V}'_i = \vec{V}_i - \vec{V}_{\mathrm{n}} = \frac{1}{1+k_i^2} \left\{ \frac{k_i}{B} \vec{E}' + \left(\frac{k_i}{B} \right)^2 \vec{E}' \times \vec{B} \right\}, \tag{A.10a}$$

$$\vec{V}'_{\mathrm{e}} = \vec{V}_{\mathrm{e}} - \vec{V}_{\mathrm{n}} = \frac{1}{1+k_{\mathrm{e}}^2} \left\{ -\frac{k_{\mathrm{e}}}{B} \vec{E}' + \left(\frac{k_{\mathrm{e}}}{B} \right)^2 \vec{E}' \times \vec{B} \right\}. \tag{A.10b}$$

Substituting these equations into Eq. (A.9) results in the expression

$$\vec{j} \cdot \vec{E}' = \sum_i q_i n_i \left(\frac{k_{\mathrm{e}}}{1+k_{\mathrm{e}}^2} + \frac{k_i}{1+k_i^2} \right) \frac{\vec{E}'}{\vec{B}} \cdot \vec{E}'$$

$$= \sigma_{\mathrm{p}} \vec{E}'^2. \tag{A.11}$$

Assuming that k_{e} is large in the ionosphere, which is true above 90 km, and rearranging terms we arrive at the expression for the Joule heating rate as

$$\vec{j} \cdot \vec{E}' = \sum_i m_i n_i \vec{\Omega}_i \left(\frac{k_i}{1+k_i^2} \right) \frac{\vec{E}'^2}{B^2}. \tag{A.12}$$

Furthermore, we can write the square of the ion velocity in the neutral wind reference frame, using the approximated ion momentum equation given in Eq. (A.10a) as

$$\frac{V_{i'}^2}{k_i} = \left(\frac{k_i}{1+k_i^2} \right) \frac{E'^2}{B^2}. \tag{A.13}$$

Substituting this expression into Eq. (A.12) results in

$$\vec{j} \cdot \vec{E}' = \sum_i n_i m_i \nu_{i\mathrm{n}} (\vec{V}_i - \vec{V}_{\mathrm{n}})^2. \tag{A.14}$$

Thus, when the above assumptions are applied, the MHD Joule heating rate is equal to the frictional heating rate. Brekke (1997) discusses other caveats of this relationship in the presence of a time-varying electric field. Thus, either term or approach can account for the change in internal energy of the neutral gas because the MHD assumption is heavily weighted towards the neutral gas in the IT system; we worked with the neutral species energy equation to show the link. However, each species can have its own frictional heating term, so that the use of this term can be confusing. For instance, frictional heating of the ion species results in a response much different from that of frictional heating of the neutral gas. To illustrate, we write below the expression for the ion temperature as derived from the approximated ion energy equation given in Eq. (A.3):

$$T_i \cong T_{\mathrm{n}} + \frac{m_{\mathrm{n}}}{3k_{\mathrm{B}}} (\vec{V}_i - \vec{V}_{\mathrm{n}})^2. \tag{A.15}$$

Here we find that the ion temperature increases according to the square of the relative drift between the ions and neutrals. Only changes in neutral mass and temperature can temper this change. In contrast, we see from the Joule heating equation (A.14) that the frictional heating rate to the neutral gas is dependent not only on the square of the relative drift between the ions and neutrals but also on the exponentially decreasing ion–neutral collision frequency with height and the time-varying total ion density (or equivalently under charge neutrality, the electron density). These variables can be appreciable factors in influencing the frictional heating rate of the neutral gas with height, while ion frictional heating does not depend on these variables and can respond quite rapidly to changes in the electric field. A good illustration of this point is given by Heelis and Coley (1988). Thus, the neutral frictional heating rate does equate to the Joule heating rate, after some reasonable assumptions, while the ion frictional heating rate does not equate to the Joule heating rate.

Symbols: The symbols used in this appendix are listed in Table 1.

References

Atkinson, G., 1970. Result of the interaction of a dynamic magnetosphere with the ionosphere. Journal of Geophysical Research 75, 4746–4754.

Banks, P.M., Kockarts, G., 1973. Aeronomy Part A. Academic Press, New York.

Barrett, J., Hays, P., 1976. Spatial distribution of energy deposited in nitrogen by electrons. Journal of Chemical Physics 64, 743.

Boström, R., 1976. Ionosphere–magnetosphere coupling. In: McCormac, B.M. (Ed.), Magnetospheric Physics. D. Reidel Publishing Company, Dordrecht-Holland, pp. 45–59.

Brekke, A., 1997. Physics of the Upper Polar Atmosphere. Praxis Publishing, Chichester.

Brekke, A., Hall, C., 1989. Auroral ionospheric conductances during disturbed conditions. Annales Geophysicae 7, 269–280.

Brekke, A., Rino, C.L., 1978. High-resolution altitude profiles of the auroral zone energy dissipation due to ionospheric currents. Journal of Geophysical Research 83 (A6), 2517–2524.

Chamberlain, J., Hunten, D., 1987. Theory of planetary atmospheres. Academic Press, San Diego.

Chapman, S., Cowling, T.G., 1970. The Mathematical Theory of Non-Uniform Gases. Cambridge University Press, New York.

Codrescu, M.V., Fuller-Rowell, T.J., Foster, J.C., Holt, J.M., Cariglia, S.J., 2000. Electric field variability associated with the Millstone Hill electric field model. Journal of Geophysical Research 105 (A3), 5265–5273.

Cowley, S.W.H., 1991. Acceleration and heating of space plasma: basic concepts. Annales Geophysicae 9, 176–187.

Dalgarno, A., 1962. Range and energy loss. In: Bates, D. (Ed.), Atomic and Molecular Processes. Academic Press, New York, pp. 622.

de la Beaujardière, O., Johnson, R., Wickwar, V.B., 1991. Ground-based measurements of Joule heating rates. Auroral Physics, 439–448.

Ergun, R., Su, Y.-J., Andersson, L., Carlson, C., McFadden, J., Mozer, F., Newman, D., Goldman, M., Strangeway, R., 2001. Direct observations of localized parallel electric fields in a space plasma. Physics Research Letters 87, 045003-1–045003-4.

Evans, D.S., Maynard, N., Trøim, J., Jacobsen, T., Egeland, A., 1977. Auroral vector electric field and particle comparisons 2. Electrodynamics of an Arc. Journal of Geophysical Research 82 (16), 2235–2249.

Fano, U., 1946. On the theory of ionization yield of radiations in different substances. Physics Review 70, 44–52.

Farley, D.T., 1959. A theory of electrostatic fields in a horizontally stratified ionosphere subject to a vertical magnetic field. Journal of Geophysical Research 64, 1225.

Fujii, R., Nozawa, S., Matuura, N., Brekke, A., 1998. Study on neutral wind contribution to the electrodynamics in the polar ionosphere using EISCAT CP-1 data. Journal of Geophysical Research 103, 14731–14739.

Fujii, R., Nozawa, S., Buchert, S.C., Brekke, A., 1999. Statistical characteristics of electromagnetic energy transfer between the magnetosphere, the ionosphere, and the thermosphere. Journal of Geophysical Research 104 (A2), 2357–2365.

Ganguli, G., Keskinen, M.J., Romero, H., Heelis, R.A., Moore, T., Pollock, C., 1994. Coupling of microprocesses and macroprocesses due to velocity shear: an application to the low-altitude ionosphere. Journal of Geophysical Research 99, 8873–8889.

Gary, J.B., Heelis, R.A., Hanson, W.B., Slavin, J.A., 1994. Field-aligned Poynting flux observations in the high-latitude ionosphere. Journal of Geophysical Research 99, 11417–11427.

Gary, J.B., Heelis, R.A., Thayer, J.P., 1995. Summary of field-aligned Poynting flux observations from DE 2. Geophysical Research Letters 22 (14), 1861–1864.

Grad, H., 1958. Principles of the kinetic theory of gases. Handbuch der Physik XII, 205–294.

Hasegawa, A., 1976. Particle Acceleration by MHD surface wave and formation of aurora. Journal of Geophysical Research 81 (28), 5083–5090.

Heelis, R.A., Coley, W.R., 1988. Global and local Joule heating effects seen by DE 2. Journal of Geophysical Research 93 (A7), 7551–7557.

Heelis, R.A., Vickrey, J.F., 1991. Energy dissipation in structured electrodynamic environments. Journal of Geophysical Research 96 (A8), 14189–14194.

Heppner, J.P., 1977. Empirical models of high-latitude electric fields. Journal of Geophysical Research 82, 1115.

Hill, T.W., 1983. Solar-wind magnetosphere coupling. In: Carovillano, R.L., Forbes, J.M. (Eds.), Solar-terrestrial Physics. D. Reidel, Norwell, MA, pp. 261–302.

Hinteregger, H.E., Fukui, K., Gilson, B.R., 1981. Observational reference, and model data on solar EUV, from measurements on AE-E. Geophysical Research Letters 8, 1147.

Kamide, Y., Kroehl, H.W., 1987. A concise review of the utility of ground-based magnetic recordings for estimating the joule heat production rate. Annales Geophysicae 5A, 535–542.

Keiling, A., Wygant, J.R., Cattell, C., Peria, W., Parks, G., Temerin, M., Mozer, F.S., Russell, C.T., Kletzing, C.A., 2002. Correlation of Alfvén wave Poynting flux in the plasma sheet at 4–7 R_E with ionospheric electron energy flux. Journal of Geophysical Research 107(A7), 10.1029/2001JA900140.

Kelley, M.C., 1989. The Earth's Ionosphere. Academic Press, New York.

Kelley, M.C., Knudsen, D.J., Vickrey, J.F., 1991. Poynting flux measurements on a satellite: a diagnostic tool for space research. Journal of Geophysical Research 96 (A1), 201–207.

Killeen, T.L., Hays, P.B., Carignan, G.R., Heelis, R.A., Hanson, W.B., Spencer, N.W., Brace, L.H., 1984. Ion–neutral coupling in the high latitude F-region: evaluations of ion heating terms from Dynamics Explorer 2. Journal of Geophysical Research 89, 7495–7508.

Kletzing, C.A., Berg, G., Kelley, M.C., Primdahl, F., Torbet, R.B., 1996. The electrical and precipitation characteristics of morning sector Sun-aligned auroral arcs. Journal of Geophysical Research 101 (A8), 17175–17189.

Knight, S., 1973. Parallel electric fields. Planetary Space Sciences 21, 741–750.

Knudsen, D.J., 1990. Alfvén waves and static fields in magnetosphere/ionosphere coupling: in-situ measurements and a numerical model. Ph.D. Thesis, Cornell University.

Kockarts, G., 1980. Nitric oxide in the terrestrial thermosphere. Geophysical Research Letters 7, 137–140.

Lanchester, B.S., Kaila, K., McCrea, I.W., 1996. Relationship between large horizontal electric fields and auroral arc elements. Journal of Geophysical Research 101, 5075–5084.

Larsen, M.F., Mikkelsen, I.S., 1983. The dynamic response of the high-latitude thermosphere and geostrophic adjustment. Journal of Geophysical Research 88 (A4), 3158–3168.

Lu, G., Richmond, A.D., Emery, B.A., Roble, R.G., 1995. Magnetosphere–ionosphere–thermosphere coupling: effect of neutral winds on energy transfer and field-aligned current. Journal of Geophysical Research 100 (A10), 19643–19659.

Lummerzheim, D., Lilensten, J., 1994. Electron transport and energy degradation in the ionosphere: evaluation of the numerical solution, comparison with laboratory experiments and auroral observations. Annales Geophysicae 12, 1039.

Lyons, L.R., Lundin, R., Evans, D.S., 1979. An observed relation between magnetic field aligned electric fields and downward electron energy fluxes in the vicinity of auroral forms. Journal of Geophysical Research 84, 457.

Lysak, R., Song, Y., 2002. Energetics of the ionospheric feedback interaction. Journal of Geophysical Research 107, 10.1029/2001JA000308.

Marklund, G., 1984. Auroral arc classification scheme based on the observed arc-associated electric field pattern. Planetary Space Science 32, 193–211.

Mayr, H.G., Harris, I., 1978. Some characteristics of electric field momentum coupling with the neutral atmosphere. Journal of Geophysical Research 83 (A7), 3327–3336.

McFadden, J., Carlson, C., Ergun, R., 1999. Microstructure of the auroral acceleration region observed by FAST. Journal of Geophysical Research 104, 14453.

Mozer, F., Hull, F., 2001. Origin and geometry of upward parallel electric field in the auroral acceleration region. Journal of Geophysical Research 106, 5763–5778.

Mozer, F.S., Cattell, C.A., Hudson, M.K., Lysak, R.L., Temerin, M., Torbert, R.B., 1980. Satellite measurements and theories of low altitude auroral particle acceleration. Space Science Review 27, 155.

Newell, P.T., Meng, C.-I., Lyons, K.M., 1996. Discrete aurorae are suppressed in sunlight. Nature 381, 766.

Newell, P.T., Greenwald, R.A., Ruohoniemi, J.M., 2001. The role of the ionosphere in aurora and space weather. Reviews of Geophysics 39 (2), 137–149.

Primdahl, F.G., Sandahl, I., 1987. Rocket observations of E-B field correlations howing up- and down-going Poynting flux during an auroral breakup event. Planetary Space Science 35, 1287.

Rees, M., 1963. Auroral ionization and excitation by incident energetic electrons. Planetary Space Science 11, 1209–1218.

Rees, M., 1989. Physics and Chemistry of the Upper Atmosphere. Cambridge University Press, Cambridge, UK.

Rees, M.H., Emery, B., Roble, R., Stamnes, K., 1983. Neutral and ion gas heating by auroral electron precipitation. Journal of Geophysical Research 88 (A8), 6289–6300.

Rich, F.J., Emery, B.A., Roble, R.G., Stamnes, K., 1987. Using simultaneous particle and field observations on a low altitude satellite to estimate Joule heat energy flow into the high latitude ionosphere. Annales Geophysicae, 527–534.

Rich, F.J., Gussenhoven, M.S., Hardy, D.A., Holeman, E., 1991. Average height-integrated Joule heating rates and magnetic deflection vectors due to field-aligned currents during sunspot minimum. Journal of Atmospheric and Solar-Terrestrial Physics 53 (3/4), 293–308.

Richmond, A.D., 1983. Thermospheric dynamics and electrodynamics. In: Carovillano, R.L., Forbes, J.M. (Eds.), Solar-terrestrial Physics. D. Reidel, Norwell, MA, pp. 523–607.

Rishbeth, H., Garriott, O.K., 1969. Introduction to Ionospheric Physics. Academic Press, New York and London.

Robinson, R.M., 1984. K_p Dependence of auroral zone field-aligned current intensity. Journal of Geophysical Research 89 (A3), 1743–1748.

Roble, R.G., Ridley, E.C., Dickinson, R.E., 1987. On the global mean structure of the thermosphere. Journal of Geophysical Research 92, 8745–8758.

St. Maurice, J.-P., Hanson, W.B., 1982. Ion frictional heating at high latitudes and its possible use for an in situ determination of neutral thermospheric winds and temperatures. Journal of Geophysical Research 87, 7580–7602.

St. Maurice, J.-P., Hanson, W.B., 1984. A statistical study of F region ion temperatures at high latitudes based on Atmosphere Explorer C data. Journal of Geophysical Research 89, 987–996.

St. Maurice, J.-P., Schunk, R.W., 1979. Ion velocity distributions in the high-latitude ionosphere. Reviews of Geophysical Space Physics 17, 99–134.

St. Maurice, J.-P., Schunk, R.W., 1981. Ion–neutral momentum coupling near discrete high latitude ionospheric features. Journal of Geophysical Research 86, 11299–11321.

Sato, T., 1978. A theory of quiet auroral arcs. Journal of Geophysical Research 83, 1042–1048.

Schunk, R.W., 1975. Transport equations for aeronomy. Planetary Space Science 23, 437–485.

Schunk, R.W., 1977. Mathematical structure of transport equations for multispecies flows. Reviews of Geophysical Space Physics 15, 429–445.

Schunk, R.W., Nagy, F., 1980. Ionospheres of the terrestrial planets. Reviews of Geophysical Space Physics 18, 813–852.

Schunk, R.W., Nagy, A.F., 2000. Ionospheres, Physics, Plasma Physics, and Chemistry. Cambridge University Press, New York.

Schunk, R.W., Sojka, J.J., 1982. Ion temperature variations in the daytime high-latitude F-region. Journal of Geophysical Research 87, 5169–5183.

Semeter, J., Doe, R., 2002. On the proper interpretation of ionospheric conductance estimated through satellite photometry. Journal of Geophysical Research 107, 10.10292001JA009101.

Siskind, D.E., Barth, C.A., Roble, R.G., 1989a. The response of thermospheric nitric oxide to an auroral storm 1. Low and middle latitudes. Journal of Geophysical Research. 94 16885–16898.

Siskind, D.E., Barth, C.A., Evans, D.S., Roble, R.G., 1989b. The response of thermospheric nitric oxide to an auroral storm 2. Auroral latitudes. Journal of Geophysical Research 94, 16899–16911.

Solomon, S.C., Hays, P.B., Abreu, V.J., 1988. The auroral 6300 Å emission: observations and modeling. Journal of Geophysical Research 93, 9867.

Solomon, S.C., Bailey, S.M., Woods, T.N., 2001. Effect of solar soft X-rays on the lower ionosphere. Geophysical Research Letters 28 (11), 2149–2152.

Strickland, D., Meier, R., Hecht, J., Christensen, A., 1989. Deducing composition and incident electron spectra from ground-based auroral optical measurements: theory and results. Journal of Geophysical Research 94, 13527–13539.

Sugino, M., Fujii, R., Nozawa, S., Buchert, S.C., Opgenoorth, H.J., Brekke, A., 2002. Relative contribution of ionospheric conductivity and electric field to ionospheric current. Journal of Geophysical Research 107(A10), doi: 10.1029/2001JA007545.

Sugiura, M., Maynard, N.C., Farthing, W.H., Ledley, J.P.H.G., Cahill, J.L.J., 1982. Initial results on the correlation between the magnetic and electric fields observed from the DE-2 satellite in field-aligned current regions. Geophysical Research Letters 9, 985.

Thayer, J.P., 1998a. Height-resolved Joule heating rates in the high-latitude E region and the influence of neutral winds. Journal of Geophysical Research 103 (A1), 471–487.

Thayer, J.P., 1998b. Radar measurements of the energy rates associated with the dynamic ionospheric load/generator. Geophysical Research Letters 25, 469–472.

Thayer, J.P., 2000. High latitude currents and their energy exchange with the ionosphere-thermosphere system. Journal of Geophysical Research 105 (A10), 23015–23024.

Thayer, J.P., Vickrey, J.F., 1992. On the contribution of the thermospheric neutral wind to high latitude energetics. Geophysical Research Letters 19 (3), 265–268.

Thayer, J.P., Vickrey, J.F., Heelis, R.A., Gary, J.B., 1995. Interpretation and modeling of the high-latitude electromagnetic energy flux. Journal of Geophysical Research 100 (A10), 19715–19728.

Tobiska, W.K., Woods, T., Eparvier, F., Viereck, R., Floyd, L., Bouwer, D., Rottman, G., White, O.R., 2000. The SOLAR2000 empirical solar irradiance model and forecast tool. Journal of Atmospheric and Solar-Terrestrial Physics 62, 1233–1250.

Torr, M.R., Torr, D.G., Richards, P.G., 1980. The solar ultraviolet heating efficiency of the midlatitude thermosphere. Geophysical Research Letters 7 (5), 373–376.

Vallance-Jones, A., 1974. Aurora. D. Reidel Publishing Company, Dordrecht, Netherlands.

Vickrey, J.F., Vondrak, R.R., Matthews, S.J., 1982. Energy deposition by precipitating particles and Joule dissipation in the auroral ionosphere. Journal of Geophysical Research 87 (A7), 5184–5196.

Zhang, S.P., Shepherd, G.G., 2002. Neutral winds and O(1S) emission rates in the lower thermosphere as measured with WINDII/UARS during the April 4–5th 1993 and February 1994 geomagnetic storms. Journal of Atmospheric and Solar-Terrestrial Physics 64, 1201–1214.